Check for updates

Solid-state *vs.* spray-drying synthesis for Mg-doped P2–Na$_{0.67}$Fe$_{0.5}$Mn$_{0.5}$O$_2$ as a cathode material for sodium-ion batteries

Mattia Canini, [iD] *[ab] Daniele Callegari, [iD] [ab] Matteo Bianchini [iD] [cd] and Eliana Quartarone [iD] [ab]

Among the different cathodes studied for Sodium-Ion Batteries (SIBs), the P2-layered oxide structure has garnered significant attention due to its electrochemical properties. However, several critical issues must still be addressed to enable large-scale commercialization, including the numerous phase transitions that the structure undergoes during cycling at high potentials (4 V) and the low Na content in the pristine material. In this work, starting from the promising and sustainable Na$_{0.67}$Mn$_{0.5}$Fe$_{0.5}$O$_2$, we developed new cathodes by partially replacing Fe with Mg. In addition to studying the role of Mg(II), a cation known for its stabilizing properties, we also evaluated the influence of two different synthesis methods on the structural and functional properties. In particular, spray-drying proved to be very promising compared to the conventional solid-state synthesis, as it leads to materials with morphology and microstructures more compatible with application as cathodes for batteries. The calculated Na diffusion coefficient (D_{Na^+}) is more than two orders of magnitude higher for P2–Na$_{0.67}$Mn$_{0.5}$Fe$_{0.3}$Mg$_{0.2}$O$_2$ prepared by spray-drying than that by the solid-state synthesis (10^{-8} *vs.* 10^{-10} cm^2 s^{-1}). In line with this result, the capacity retention after 100 cycles @ 1C is also significantly higher (72% *vs.* 81%). Compared with P2–Na$_{0.67}$Mn$_{0.5}$Fe$_{0.5}$O$_2$, Mg(II)-doping significantly improves the cathodic performances of the spray-dried materials, increasing capacity retention after 200 cycles at 1C from 39% to 69%. In conclusion, we confirmed that the choice of the correct synthesis route, combined with optimization of elemental composition, plays a crucial role in the development of high performance materials for SIBs.

1. Introduction

In recent years, the energetic transition and the research on new electrochemical energy storage devices that can compete with lithium-ion batteries (LIBs) led to the development of new types of batteries based on different elements, such as Na$^+$, K$^+$, Ca^{2+}, or Mg^{2+}.[1–5] Among them, Sodium-Ion Batteries (SIBs) represent one of the most viable and promising alternatives to LIBs in terms of (i) sustainability, since they don't need critical raw materials such as Li, Co, and graphite for their production; (ii) abundance of Na resources in the Earth's crust and in sea or industrial waters; (iii) safety, since it has been verified that full SIBs can be stored and transported safely and without compromising their performance even at 0 V, unlike LIBs that can never be stored at such low voltages.[6,7] On the other hand, due to its intrinsic properties, Na has some disadvantages compared to Li in terms of lower energy density (both volumetric and gravimetric) and higher standard reduction potential (−2.7 V and −3.0 V for Na$^+$/Na and Li$^+$/Li, respectively). Considering this limitation, it is essential to harness the specific advantages of both battery technologies to broaden the range of energy storage solutions and decrease reliance on LIBs. Consequently, SIBs should be regarded as complementary to LIBs, particularly in applications where high energy density and power within a compact design are not primary requirements (*e.g.*, electric vehicles).[8] In recent years, world-leading companies in the field have been investing in developing sodium-ion batteries, in some cases already reaching large-scale production and commercialization. Prominent among these is China's CATL, which in 2021 presented its first battery based on Prussian white (cathode) and hard carbon (anode), with an energy density > 160 Wh kg^{-1}.[9] In Europe, an example is Britain's Faradion, which bases its battery on layered oxide-type cathodes and hard carbon-based anodes, with energy density > 120 Wh kg^{-1} and an average life of more than 3000 cycles.[10] The French Tiamat uses polyanionic compounds as cathodes and patented batteries with energy densities of 90–120 Wh kg^{-1}, super-fast

aDepartment of Chemistry, University of Pavia, Viale Taramelli 12, 27100 Pavia, Italy. E-mail: mattia.canini01@universitadipavia.it

bNational Interuniversity Consortium of Materials Science and Technology (INSTM), Via G. Giusti 9, 50121 Firenze, Italy

cDepartment of Chemistry, Biology and Geosciences, Universität Bayreuth, Universitätsrasse 30, 95447 Bayreuth, Germany

dBavarian Center for Battery Technology (BayBatt), Universität Bayreuth, Weiherstrasse 26, 95448 Bayreuth, Germany

charge (5 minutes), and an average life of more than 5000 cycles with capacity retention > 80%.[11] The choice of the cathode material is one of the crucial steps in the design of sustainable SIBs.[12] For example, one of the main advantages of layered oxides is the possibility of achieving high energy densities by appropriately choosing their composition, even though this often comes at the expense of long-term stability.[13,14] For polyanionic compounds, the trend is the opposite; because of their high molecular weight, they do not guarantee high energy densities, but they have high structural stability even after being stressed for many cycles. Prussian blue analogs, finally, have intermediate properties between those of the previous two in terms of energy density and stability but have the great advantage of having much lower production costs. On the other hand, their safety is still under debate.[15] Unlike the most widely used cathode for lithium-ion batteries, lithium cobalt oxide $LiCoO_2$ (LCO),[16,17] whose layered structure can only be of the O3 type (space group $R\bar{3}m$), layered cathodes for SIBs can be synthesized in different stacking sequences, among which the most important are P2 (space group $P6_3/mmc$) and O3. As proposed by Delmas et al.,[18] the letters P and O represent the coordinative environment of Na^+ ions, prismatic and octahedral, respectively; the numbers indicate how many Na layers are present in each elementary cell. These two phases have different initial sodium content and markedly different electrochemical performances. P2 generally offers higher ionic conductivity and structural stability than O3. However, at high potentials (>4 V), it suffers from phase transitions to other phases (named O2, OP4, or Z in the literature), which are often electrochemically inactive.[19,20] O3, by contrast, has a higher specific discharge capacity (due to its higher Na^+ content), but it has slower Na^+ diffusion kinetics and a lower average potential than P2. Even though this depends on the exact composition, all the layered structures are air-sensitive[21] but, in general, O3 phases suffer from more structural distortions than P2 ones when exposed to air or humidity.[22] One of the most promising research activities on layered oxides is trying to enhance their cathodic performance by modifying the elemental compositions, by introducing electrochemically inactive cations known for their stabilizing properties like Mg^{2+}, Ca^{2+}, or Ti^{4+}.[23–25] Mg^{2+} sits on the lattice site occupied by the active cations on the transition metal layers and, because of this, it can prevent the collapse and slippage of the planes during cycling.[26–28] In addition, Mg^{2+} also allows for increased P2-layered oxide air stability by increasing the average oxidation state of the other cations in the structure.[14,29]

Among the various compositions studied and reported in the literature, $P2-Na_{0.67}Mn_{0.5}Fe_{0.5}O_2$ is certainly one of the most promising, due to its favorable electrochemical properties (theoretical energy density of 520 Wh kg^{-1}) and low production cost, resulting from the natural abundance of both Mn and Fe. However, the aforementioned phase transitions at high voltages limit its large-scale application. Various synthesis strategies[30,31] and cation substitutions have demonstrated that optimizing these two factors can significantly enhance cathode performance. For instance, a slight substitution with Ti^{4+} or Si^{4+}

increases capacity retention by nearly 50% compared to the unsubstituted oxide after 100 cycles.[32,33]

Recently, the development of layered cathodes with a P2/O3 biphasic structure has garnered significant attention, as this configuration combines the advantages of both phases, yielding higher-performance cathodes compared to pure P2 or O3. As an example, Faradion has successfully commercialized a P2/O3 biphasic cathode with the composition $Na_xNi_{1-x-y-z}Mg_xMn_yTi_zO_2$, demonstrating enhanced electrochemical properties compared to their first pure O3 materials.[10]

The synthesis route plays a key role in the development of electrode materials, as depending on the precursors used and the synthesis conditions, materials with the same composition but different cathodic performances can be obtained due to a different morphology, porosity, and microstructure. Spray-drying or spray-pyrolysis, for example, represents some of the most promising types of synthesis, as they are low-cost, highly reproducible, and easily scalable.[34–36] Experimentally, spray-drying synthesis consists of three parts: (i) atomization of the starting solution into fine droplets; (ii) evaporation of the solvent (usually H_2O) by a hot gas flow; (iii) recovery of the dry powder, with the desired composition and regular morphology. In many cases, final calcination at high temperatures (700–800 °C) is also necessary for the formation of the desired crystalline structure.

In this work, we synthesized and characterized P2-layered oxide cathodes for sodium batteries with stoichiometry $Na_{0.67}Mn_{0.5}Fe_{0.5-x}Mg_xO_2$ ($x = 0, 0.2$). Starting from the already known $P2-Na_{0.67}Mn_{0.5}Fe_{0.5}O_2$ oxide, we evaluated the stabilizing role imparted by doping with Mg^{2+} on the cathodic performance, both from the performance point of view and by evaluating the diffusion coefficient D_{Na^+} during cycling. The structural evolution of the materials was evaluated during cycling by *operando* XRD experiments. In addition, both compositions were prepared by both solid-state synthesis and spray-drying synthesis; hence we could evaluate the influence of synthesis conditions on the morphological, structural, and electrochemical properties of all materials.

2. Materials and methods

2.1. Synthesis of $P2-Na_{0.67}Mn_{0.5}Fe_{0.5-x}Mg_xO_2$ ($x = 0, 0.2$)

$P2-Na_{0.67}Mn_{0.5}Fe_{0.5-x}Mg_xO_2$ ($x = 0, 0.2$) were prepared through solid-state synthesis (SS-0 and SS-02), starting from commercial oxides and Na_2CO_3 in an appropriate stoichiometric ratio. To increase the contact area between the particles, all the precursors were first mixed in stainless steel jars using a planetary ball miller at 100 rpm for 3 h. Sodium carbonate was introduced in 5 wt% excess to compensate for the eventual loss of Na after high-temperature calcination. Subsequently, the resulting powder was sintered in pellets, using a uniaxial press, and treated in a tube furnace at 1000 °C for 3 h (ramp rate of 5 °C min^{-1}), at the end of which the structure was quenched by quickly removing the product from the furnace to avoid phase transitions during cooling time.

The two compositions were also synthesized by spray-drying synthesis (SD-0 and SD-02) followed by heat treatments. For the

spray-dry process, we used a Buchi Mini Spray Dryer B-290, starting from a 0.2 M water solution made of commercial $Fe(NO_3)_3 \cdot 9H_2O$, $(CH_3COO)_2Mn \cdot 4H_2O$, $Mg(NO_3)_2 \cdot 6H_2O$ and $CH_3COONa \cdot 3H_2O$. Since this synthesis allowed us to reduce the synthesis temperature, we didn't expect Na loss during the calcination process, so we didn't introduce Na excess. Table S1 shows the conditions imposed on the instrument for the spray process. After collecting the resulting spray-dried powder, we calcined it at 775 °C for 8 h (SD-0) and 800 °C for 10 h (SD-02) for P2-layered phase formation.

2.2. Cathode preparation and cell assembly

The cathode slurry was prepared by using 80 wt% of active material, 10 wt% of conductive carbon black (Imerys, Ensaco 350P), and 10 wt% of a binder (polyvinylidene fluoride, PVdF). The solid content of all slurries was kept between 28 wt% and 30 wt%. The Cathode Active Material (CAM) and carbon powders were mixed in zirconia jars using a planetary ball mill at 150 rpm for 10 min twice, with a rest period of 5 min. Subsequently, the polymeric binder was added and mixed in a similar procedure. The as-prepared mixture was dispersed in N-methyl pyrrolidone (NMP) to obtain the slurry, which was cast on carbon-coated Al foil using a doctor blade with a wet thickness of 300 μm. The cast slurry was dried under vacuum at 80 °C to avoid moisture and oxygen contamination. The cathode was finally cut into 2 cm² disks and stored in an Ar-filled glove box (MBraun, O_2, H_2O < 0.5 ppm) before the electrochemical measurements. The loading of the electrodes was ~3 mg cm⁻². For operando XRD experiments, we prepared the electrodes following a different procedure, as reported elsewhere.[37] All the functional tests were performed in coin cells (CR2032-MTI Corp.) assembled in an inert atmosphere (Ar) at room temperature (25 °C). Metallic Na was used as the counter electrode. Electrodes were separated with two Whatman GF/A glass fiber separators, imbibed by 90 μL of liquid electrolyte, consisting of a solution of 1 M $NaPF_6$ in ethylene carbonate: dimethyl carbonate + 2 wt% fluoroethylene carbonate (FEC).

2.3. Characterization

Morphologies and elementary compositions of the materials were investigated through SEM and ICP-AES analysis. We used a Tescan Mira3 XMU microscope operated at 20 kV and equipped with an EDAX EDX analysis system and a Thermo Fisher Scientific Phenom ProX microscope to collect SEM images. ICP-OES analyses were performed using an Avio 220 max (PerkinElmer), equipped with an AVIO Glass Cyclonic Baffled spray chamber, a quartz torch, and a dual backside-illuminated charge-coupled device (DBI-CCD) detector. The TM quantification was carried out on HNO_3-digested solutions in the axial mode at a 670.8 nm wavelength, using an external standard calibration curve. An ICP grade multi-element standard (1000 mg L⁻¹) was diluted to 0.3–0.6–2.0–5.0–9.0 mg L⁻¹ and then acidified to a final concentration of 2% nitric acid (from ultrapure 65% HNO_3). The measurement conditions were as follows: nebulization gas flow: 0.7 L min⁻¹; power RF: 1500 W; auxiliary gas flow: 0.2 L min⁻¹; peristaltic pump: 1

mL min⁻¹; frequency: 500 Hz. For Na quantification, we used ultrapure H_2O for chromatography (Na < 200 ppb).

XRD patterns of P2–$Na_{0.67}Mn_{0.5}Fe_{0.5-x}Mg_xO_2$ powder were collected with a STADI P diffractometer (STOE, Germany) with Mo-Kα1 radiation (λ = 0.70932 Å, 50 kV, and 40 mA) and a Mythen2K detector, in the 5–70° 2θ range and with a 0.015° step. Rietveld refinement was conducted using the FullProf Suite software. Operando XRD experiments were performed on a customized CR2032 coin cell with quartz glass windows (6 mm in diameter and 100 μm in thickness). The cell was mounted on a rocking sample holder in the diffractometer mentioned above and measured in transmission geometry. Each scan was recorded for 15 min in 0.015° steps from 3° to 36°. The half-cell was cycled at 0.067C. The electrochemical performances of all the materials were investigated with a Bio-Logic VMP-3e through Galvanostatic Cycling with Potential Limitation (GCPL) at different C-rates, Potentiodynamic Cycling with Galvanostatic Acceleration (PCGA), and Galvanostatic Intermittent Titration Technique   https://www.metrohm.com/en/applications/application-notes/autolab-applikationen-anautolab/an-bat-003.html (GITT) in the working potential window 1.5–4.2 V. The theoretical capacity was calculated to be 260 mA h g⁻¹ for x = 0 and 280 mA h g⁻¹ for x = 0.2, based on the molecular weight of the respective compositions and assuming, in excess, the reversible extraction of one Na^+ equivalent for each half-cycle.

3. Results and discussion

3.1. Structural and elementary analysis

XRD patterns collected on the obtained powders are reported in Fig. 1. These confirm that both solid-state and spray-drying synthesis led to the formation of materials with the desired P2-layered structure with small impurity phases. Rietveld refinement revealed that, for solid-state synthesized cathodes (Fig. 1a and b), this impurity consists of electrochemically inactive spinel-like $MnFe_2O_4$ (space group: $Fd\bar{3}m$). For spray-dried compositions (Fig. 1c and d), on the other hand, the secondary phase was found to be the electrochemically active O3-layered oxide structure (space group: $R\bar{3}m$). The presence of the O3 phase may be attributed to inhomogeneous mixing of sodium acetate during the spray process, which likely led to the formation of Na-rich and Na-poor domains, thereby favoring the formation of the O3 and P2 phases, respectively, during calcination. Tables 1 and 2 summarize the results obtained from the Rietveld refinement of structural models performed against the experimental powder XRD patterns. For these analyses, the occupancy of Mn and Fe atoms was fixed at their stoichiometric values due to the inability of X-ray diffraction to differentiate between them. We applied the same constraint also for Mg-doped samples, assuming that all Mg atoms substituted Fe on the 2a site. As indicated by the statistic factor reported under each table and the difference between the experimental and calculated profiles (blue line in Fig. 1), the refinement quality for the two x = 0 cathodes is notably lower than that for x = 0.2. This difference is attributed to stacking faults along the $\{10l\}$ family of planes in the P2–
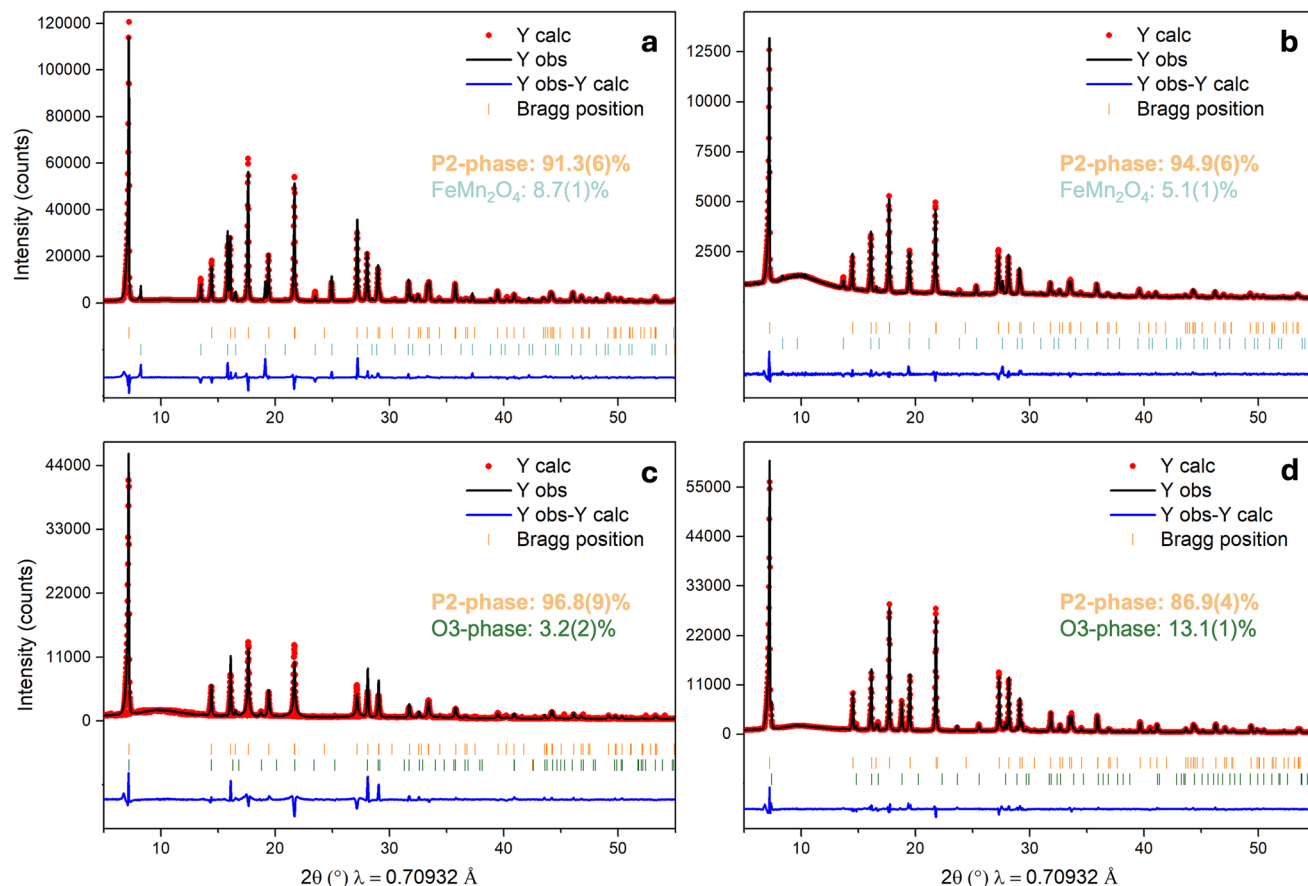
Fig. 1 Rietveld refinement of the XRD pattern of (a) SS-0, (b) SS-02, (c) SD-0, and (d) SD-02. The quantification of the P2-layered oxide and the secondary phase, obtained through the refinement, is also reported for all samples.

$Na_{0.67}Mn_{0.5}Fe_{0.5}O_2$ layered structure, as described by Yabuuchi *et al.*[38] Because of this structural defect, we decided not to refine the Na thermal factor (B_{iso}), but instead fixed it at 3.0 for SS-0 and SD-0 (Tables 1, a and 2, a). This value was selected based on the B_{iso} refinement results for $x = 0.2$ (Tables 1, b and 2, b), which do not appear to suffer from a significant amount of

Table 1 Refined structural parameters of solid-state synthesized P2-layered oxides

Atom	Multiplicity	x	y	z	B	Occ.
(a) SS-0[a]						
O	4f	1/3	2/3	0.0905(3)	0.64(7)	1.0
Fe	2a	0	0	0	0.50(2)	0.5
Mn	2a	0	0	0	0.50(2)	0.5
$Na_f(1)$	2b	0	0	1/4	3.0	0.200(5)
$Na_e(2)$	2d	1/3	2/3	3/4	3.0	0.385(6)
(b) SS-02[b]						
O	4f	1/3	2/3	0.0873(3)	0.92(6)	1.0
Fe	2a	0	0	0	0.60(2)	0.3
Mn	2a	0	0	0	0.60(2)	0.5
Mg	2a	0	0	0	0.60(2)	0.2
$Na_f(1)$	2b	0	0	1/4	3.2(2)	0.210(4)
$Na_e(2)$	2d	1/3	2/3	3/4	3.2(2)	0.391(5)

[a] Space group: $P6_3/mmc$ (194), $a = b = 2.92557(3)$ Å, $c = 11.2685(2)$ Å, $\alpha = \beta = 90°$, $\gamma = 120°$ vol. $= 83.525(2)$ Å^3. $R_p = 9.38\%$, $R_{wp} = 15.0\%$, $R_{exp} = 2.22\%$, Bragg R-factor $= 6.32\%$. [b] Space group: $P6_3/mmc$ (194), $a = b = 2.91543(3)$ Å, $c = 11.2356(2)$ Å, $\alpha = \beta = 90°$, $\gamma = 120°$ vol. $= 82.705(2)$ Å^3. $R_p = 4.44\%$, $R_{wp} = 6.13\%$, $R_{exp} = 4.62\%$, Bragg R-factor $= 3.51\%$.

Table 2 Refined structural parameters of spray-drying synthesized P2-layered oxides

Atom	Multiplicity	x	y	z	B	Occ.
(a) SD-0[a]						
O	4f	1/3	2/3	0.0831(4)	0.5(1)	1.0
Fe	2a	0	0	0	0.56(2)	0.5
Mn	2a	0	0	0	0.56(2)	0.5
$Na_f(1)$	2b	0	0	1/4	3.0	0.227(6)
$Na_e(2)$	2d	1/3	2/3	3/4	3.0	0.261(7)
(b) SD-02[b]						
O	4f	1/3	2/3	0.0905(2)	1.04(4)	1.0
Fe	2a	0	0	0	0.66(1)	0.3
Mn	2a	0	0	0	0.66(1)	0.5
Mg	2a	0	0	0	0.66(1)	0.2
$Na_f(1)$	2b	0	0	1/4	2.5(1)	0.212(2)
$Na_e(2)$	2d	1/3	2/3	3/4	2.5(1)	0.380(3)

[a] Space group: $P6_3/mmc$ (194), $a = b = 2.91998(5)$ Å, $c = 11.2921(4)$ Å, $\alpha = \beta = 90°$, $\gamma = 120°$ vol. $= 83.381(4)$ Å^3. $R_p = 9.57\%$, $R_{wp} = 13.4\%$, $R_{exp} = 3.33\%$, Bragg R-factor $= 8.76\%$. [b] Space group: $P6_3/mmc$ (194), $a = b = 2.91269(2)$ Å, $c = 11.2012(1)$ Å, $\alpha = \beta = 90°$, $\gamma = 120°$ vol. $= 82.297(1)$ Å^3. $R_p = 5.30\%$, $R_{wp} = 7–36\%$, $R_{exp} = 3.06\%$, Bragg R-factor $= 3.55\%$.

stacking faults and thus allows us to refine Na B_{iso} with good accuracy. Contrary to the expectation that Mg^{2+} doping would increase the c lattice parameter due to its larger ionic size compared to Fe^{3+}, Mn^{3+} and Mn^{4+} (0.72 Å vs. 0.64 Å, 0.64 Å and 0.53 Å, respectively), we observed a notable reduction of this parameter from 11.2685(2) Å to 11.2356(2) Å and from 11.2921(4) Å to 11.2012(1) Å for solid-state and spray-drying synthesis, respectively. The decrease in the c parameter between the materials is not attributed to the Mg(II) substitution but, instead, to a different Na^+ content within the layers of the P2-layered structure, as we will discuss later regarding the ICP analysis results. In particular, a higher Na^+ positive charge can more effectively shield the O^{2-} negative charge located in the transition metal layers, enhancing the overall attraction between the layers and, thus, promoting the contraction of the elementary cell along the c axis. The $a = b$ parameter also decreases, which we can explain due to the increased oxidation state of Mn^{3+} following the introduction of Mg^{2+}, resulting in an overall reduction in the average ionic radius of the cations.

Through ICP-OES analysis, we checked the elementary composition of all the materials under investigation. Table 3 summarizes the results of this analysis, which confirmed the good agreement between the nominal and experimental stoichiometric coefficients for all elements, except for Na.

The sodium content in all compositions is consistently lower than the theoretical value of 0.67, likely due to Na loss during high-temperature calcination. Since the Na content is recognized as one of the most influential factors affecting the structural–electrochemical properties of this family of cathode materials, we tried to accurately assess the stoichiometry of the cathodes by comparing the ICP-OES and Rietveld refinement results for the Na quantification, as summarized in Table 4 and Fig. S3.

In general, we observe a reasonable agreement between the ICP and XRD results, which improves, however, for SD samples over SS samples, and further for Mg-doped samples vs. undoped ones. The poor agreement in the case of undoped SD may be due to the stacking faults issue previously discussed, so that the Na quantification derived from the Rietveld refinement is expected to be less reliable than that obtained by ICP-OES, particularly for the $x = 0$ samples. Therefore, for all characterization studies, we considered only the Na content obtained from ICP-OES analysis. It is also worth noting that, in the case of SD-0, the sodium content is probably strongly correlated with the quality of the powder after the spray-drying process. This is likely due to a certain amount of sodium acetate not being well incorporated, resulting in a highly hygroscopic product that is, due to this reason, also difficult to collect from the spray dryer. In contrast, for SD-02, none of these issues were experimentally observed, and in fact, the final powder exhibited a significantly higher sodium content.

The morphology of all the materials under investigation was evaluated through SEM analysis. Fig. 2, related to the solid-state synthesized materials, shows micrometer-sized and very compact grains, typical of the products of reactions carried out at high temperature (1000 °C).

Spray-dried materials have a similar morphology to the one just described because of the high-temperature treatments following the spray process. However, the average size distribution (Fig. S1) showed that spray-drying synthesis led to smaller grains with a narrower distribution of dimensions, as well highlighted by the standard deviation associated with every result. The observed difference is attributable to the nature of the precursors used in the calcination process. Commercial oxides were used in solid-state synthesis, whereas a powder obtained from the spray process was employed for the spray-drying. This powder exhibits a uniform shape and size, as illustrated in Fig. 3a and c. Furthermore, EDX analysis (Fig. S2) further confirms that these particles possess the correct stoichiometric ratio of transition metals.

3.2. Electrochemical performances

All the materials were tested as positive electrode materials for SIBs in a half-cell vs. $Na_{(m)}$. Based on the literature and the composition of the oxides under investigation, we studied the electrochemical performances between 1.5 V and 4.2 V. We introduced 2 wt% FEC into the electrolyte mixture used to limit electrolyte degradation at high potentials (>4 V) during cycling.[39,40]

We evaluated the active redox phenomena from differential capacity curves (dQ/dV) obtained through PCGA analysis at low current density @ 0.067C (Fig. 4). As highlighted in the figures, two reversible active phenomena were identified in all the materials at potentials of 2–2.2 V and 3.3–4 V, corresponding to the Mn(III)/Mn(IV) and Fe(III)/Fe(IV) redox-active couples, respectively.[41] The irreversibility observed after the first charge at potentials > 4 V can be attributed in part to the degradation of the electrolyte, which is only mitigated by the presence of FEC, but also possibly to the partially irreversible oxygen redox active contribution (O^{2-}/O^-),[42,43] which we will also discuss later in the operando XRD results section. For solid-state synthesized cathodes (Fig. 4a and b), the peaks associated with active redox

Table 3 Experimental stoichiometric coefficients obtained from ICP-OES analysis for Fe, Mn and Mg

	Solid-state		Spray-drying	
	$x = 0$	$x = 0.2$	$x = 0$	$x = 0.2$
Mn	0.465	0.509	0.452	0.511
Fe	0.468	0.296	0.472	0.291
Mg	—	0.189	—	0.229

Table 4 Comparison of Na content of all the cathodes under investigation derived from ICP-OES analysis and Rietveld refinements (XRD)

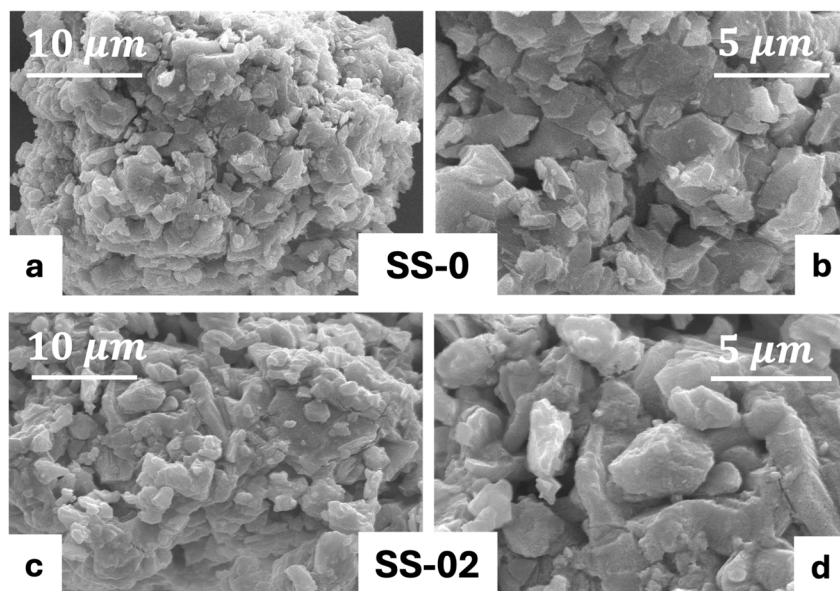|	Solid-state		Spray-drying	
	ICP-OES	XRD	ICP-OES	XRD
$x = 0$	0.491	0.59(1)	0.449	0.49(1)
$x = 0.2$	0.565	0.601(9)	0.607	0.592(5)

Fig. 2 SEM images of (a and b) SS-0 and (c and d) SS-02 at different magnifications.

phenomena appear sharper and more defined than those observed for SD-0 and SD-02 (Fig. 4c and d). In the 1st cycle, the peaks between 2.7 V and 3 V can be attributed to the polarization of the coin cell immediately after the start of the experiment.

We investigated the Na^+ content evolution in the P2 structure during the first three charge–discharge cycles for all the cathodes, aiming to assess the reversibility of the intercalation–deintercalation reaction (Fig. S4). Starting from the nominal value of Na^+ in the cathodes ($x = 0.67$), during the first charge, all materials are desodiated to a sodium content of $x = 0.2$–0.4. Over the next discharge, on the other hand, Na^+ intercalation occurs to $x = 0.8$–0.9. This sodium excess compared to the initial value is due to the $Na_{(m)}$ used as a counter-electrode, which ensures an almost infinite Na^+ source, leading to deep

sodiation of the cathodes. It's interesting to note that, in the first cycle, spray-dried cathode curves have smoother profiles than the solid-state ones. SD-02 (Fig. S4d) intercalates less Na^+ than the others, but the process is almost completely reversible over the cycles investigated. As already known in the literature, the small phenomenon observed in discharge at potentials less than 2 V (circled in blue in Fig. S4) can be attributed to the reversible passivation of the $Na_{(m)}$ counter electrode due to the presence of EC in the electrolyte mixture.[44,45] By comparing the cathodic performance of SS and SD materials (Fig. S5a and b, respectively), we confirmed the stabilizing effects of Mg^{2+} doping, regardless of the synthesis method. At all the tested C-rates and for both the synthesis routes, $x = 0.2$ discharge capacity consistently exceeds that of $x = 0$. Coulombic efficiency (C.E.) remains above 95% across all the different current
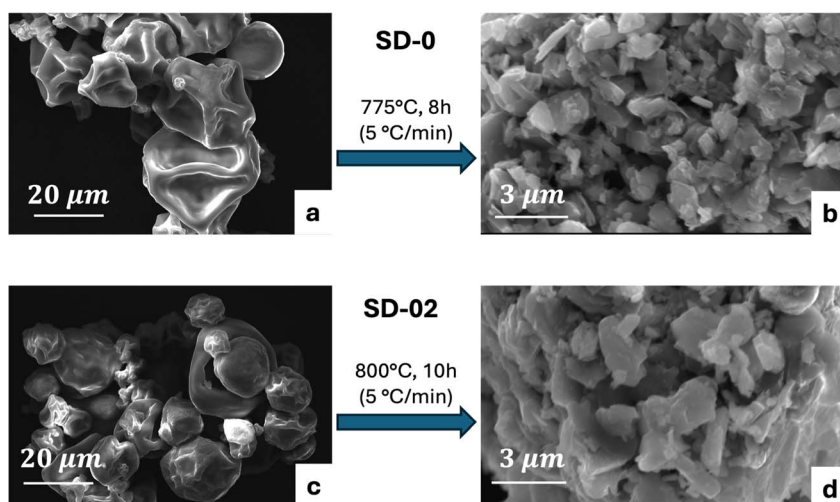

Fig. 3 SEM images of (a and b) SD-0 and (c and d) SD-02 pre- and post-heat treatments.

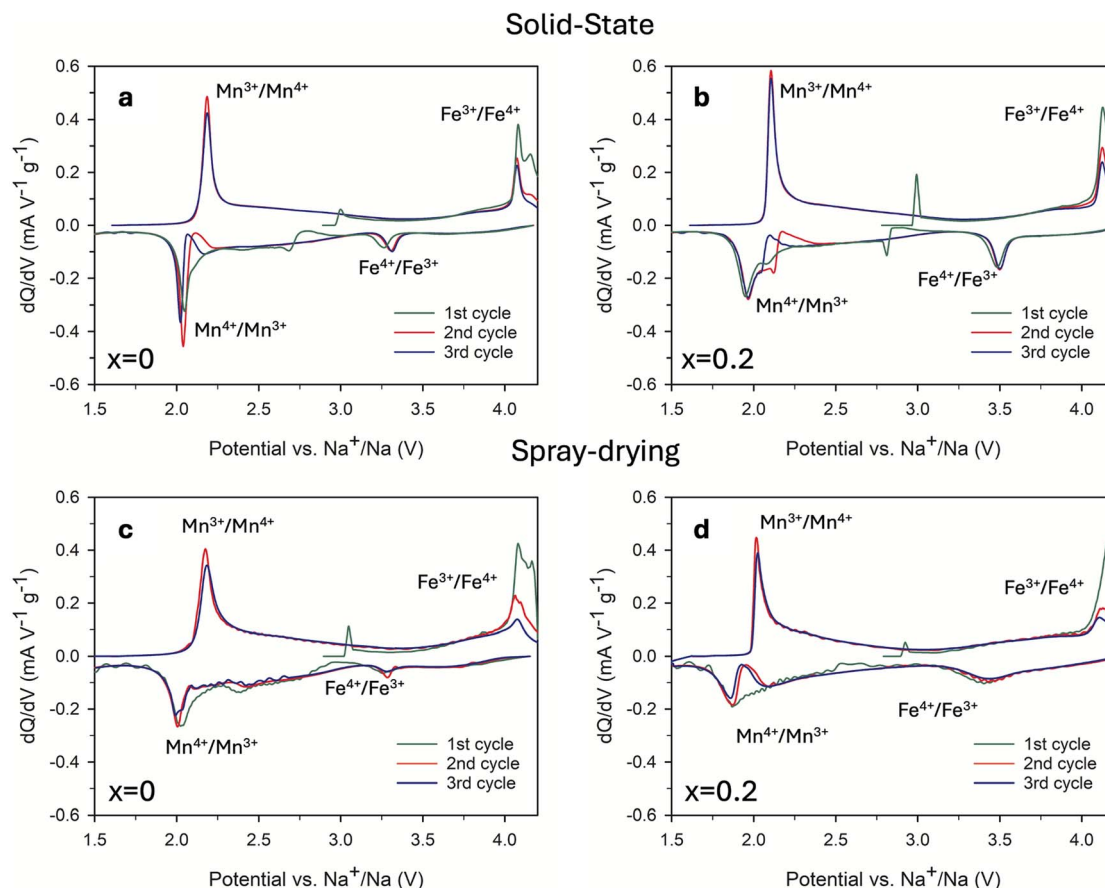## Solid-State

Spray-drying

Fig. 4   dQ/dV curves for (a) SS-0, (b) SS-02, (c) SD-0, and (d) SD-02 performed between 1.5 V and 4.2 V @ 0.067C.

densities investigated. To assess the influence of synthesis conditions on the performance, we compared the cathodic properties between SS-0 and SD-0 and between SS-02 and SD-02 (Fig. 5a and b, respectively). This comparison reveals that for both $x = 0$ and 0.2, spray-drying led to superior cathodic performance than solid-state synthesis. The good specific capacity recovery following cycles at 0.5C confirms the structural stability of all the materials, regardless of the type of synthesis. Interestingly, for the same elemental composition,

the difference in capacity observed between the two synthesis methods is significantly more pronounced for $x = 0$ than for $x = 0.2$. This difference highlights that, for the unsubstituted oxide, whose composition is not optimized through Mg(II) doping, the choice of the synthesis method leads to a marked performance improvement. As already mentioned in the Introduction, the microstructure of spray-dried materials is indeed more suitable for application in battery cathodes compared to that of solid-state materials. On the other hand, although $x = 0.2$ shows
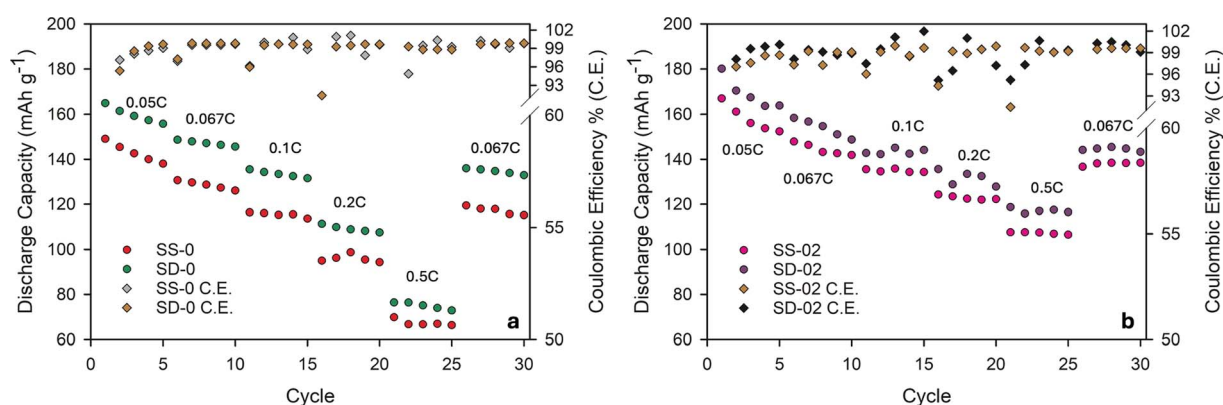

Fig. 5   GCPL experiment results on the cathodes under investigation at different C-rates between 1.5 V and 4.2 V. Comparison of discharge capacity and Coulombic Efficiency (C.E.) between (a) SS-0 and SD-0 and (b) SS-02 and SD-02.

a lower performance enhancement between the two synthesis methods compared to $x = 0$, the discharge capacities achieved with both synthesis approaches are considerably higher. Therefore, it can be concluded that Mg(II) substitution exerts a generally more impactful stabilizing effect than the choice of the synthesis route. However, it is essential to keep in mind that scan rate tests provide valuable insights during the early characterization of a material, particularly for understanding behavior at different current densities. Still, these tests alone are insufficient for the comprehensive evaluation of a new material. In order to gain deeper insight into the material properties and to further stress the layered structure of the different cathodes, with the aim of better highlighting the stabilizing effect of Mg^{2+} over cycling and the differences in performances between different syntheses, we conduct long tests (100 cycles) at a high C-rate (1C). Before cycling at 1C, we performed six pre-cycles at lower current densities (2 cycles at 0.13C, 2 cycles at 0.25C, and 2 cycles at 0.5C) to better stabilize the materials' structure and the cathode electrolyte interface.

Fig. 6 compares the average discharge capacity and coulombic efficiency (calculated over two tests performed on each sample) for the two compositions prepared by both synthesis routes. For $x = 0$ (Fig. 6a), the calculated capacity retention after 100 cycles is 50% for SD-0 and 44% for SS-0. Coulombic efficiency remained consistently high (>95%) for both cathodes. The differences in the Mg-doped oxides (Fig. 6b) are more pronounced: after 100 cycles, capacity retention is

81% and 72% for SD-02 and SS-02, respectively. Moreover, the coulombic efficiency was consistently maintained above 99% for both cathodes. The differences in discharge capacity across the two different synthesis methods employed, at the same compositions, corroborate that the Mg(II)-doping exerts a greater influence on cathodic performance than the choice of the synthesis route, in agreement with the rate capability tests results. In particular, for $x = 0.2$, the difference in capacity retention is nearly twice that of the undoped oxide, clearly indicating that the combination of an appropriate synthesis method with the stabilizing effect of Mg(II) represents a highly effective strategy for the development of high-performance cathode materials, as it leverages the advantages of both optimization approaches.

In light of these results, to further stress the electrochemical stability of the spray-dried materials, we extended the stability test to 200 cycles at 1C (Fig. 6c): the capacity retention calculated after 200 cycles increases from 39% for SD-0 to 68% for SD-02. In this regard, we confirmed what was reported by Zhou et al.[46] about the stabilizing role of the co-existence of P2/O3 compared to the pure P2-phase.

By comparing the results achieved for our best material (SD-02) with those in similar studies reported in the literature, we noticed that it's very promising in terms of performance. P2/O3 usually led to higher performances than the single P2 or O3 phase. For example, P2/O3–$Na_{0.85}Ni_{0.34}Mn_{0.33}Ti_{0.33}O_2$ demonstrated a capacity retention of 80% after 200 cycles at 1C,[47] while
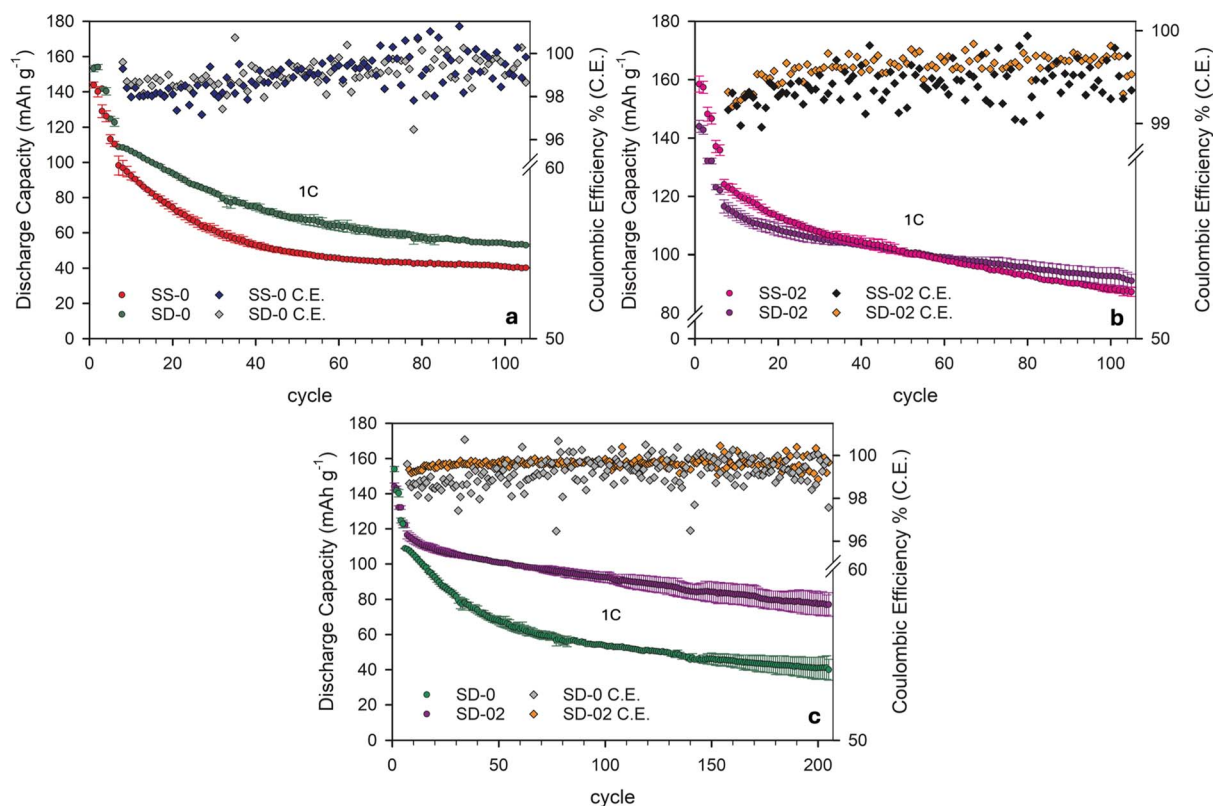

Fig. 6 Long-term cycling test @ 1C. Comparison between discharge capacity and coulombic efficiency for (a) SS-0 and SD-0, (b) SS-02 and SD-02, and (c) SD-0 and SD-02.

the High Entropy Oxide (HEO) with composition $P2-Na_{0.85}-Li_{0.08}Mg_{0.04}Ni_{0.22}Al_{0.04}Mn_{0.62}O_2$ showed 72% retention after 200 cycles at 150 mA g^{-1}, due to the high configurational entropy that helps stabilize cathodic properties during cycling.[48] The nature of the dopant cation also plays a crucial role in determining performance. For instance, $Na_{0.67}Fe_{0.5}Mn_{0.45}Al_{0.05}O_2$ exhibited excellent stability, maintaining over 90% of its initial capacity after 200 cycles at 1C,[49] mainly because of the Al^{3+} role in suppressing the Jahn–Teller distortion associated with Mn^{3+} presence. Overall, the electrochemical performance of SD-02 appears highly promising and in line with the best results reported in the literature.

We also conducted GITT experiments (see Fig. 7) to gain a clearer understanding of the intrinsic differences between materials with identical compositions but prepared through different synthesis routes by examining the evolution of the sodium diffusion coefficient (D_{Na^+}) during cycling. The D_{Na^+} was calculated using the equation below, derived by Weppner et al.[50]

$$D = \frac{4}{\pi\tau}\left(\frac{n_m V_m}{S}\right)^2\left(\frac{\Delta E_s}{\Delta E_t}\right)^2$$

where τ is the current impulse duration, n_m and V_m refer to the moles of the cathode active material and the molar volume of the active material, respectively, and S indicates the electrode surface area. Note that S should represent the active surface area of the electrode material in contact with the electrolyte, but due to the difficulty in estimating the actual surface area in a composite with a binder and carbon, we approximate it by using the electrode surface. ΔE_s and ΔE_t represent the transient voltage change during the single current pulse and the equilibrium (steady-state) potential, excluding the IR drop.

Fig. 7a and b show the charge–discharge profiles (2nd cycle) recorded for the four materials under investigation. The analysis of these curves allows for a qualitative assessment of cathode kinetics by evaluating the overpotential (η), calculated as the difference between the potential at the end of the current pulse and the end of the relaxation period.[51,52] This parameter is particularly insightful in the voltage regions corresponding to the $Fe(II)/Fe(III)$ and $Mn(II)/Mn(III)$ redox activity. Notably, the lower η observed in SD-02 compared to SS-02 indicates superior and faster kinetics.

As reported in Fig. 7c and d, the diffusion coefficient trend shows significant decreases in the voltage regions where electrochemically active phenomena occur for all the materials under investigation. However, the GITT cannot be deemed reliable at these potentials because the approximations made for calculating D_{Na^+} only apply when the materials exhibit solid-solution-like behavior.[53] In particular, Fig. 7c shows that SS-
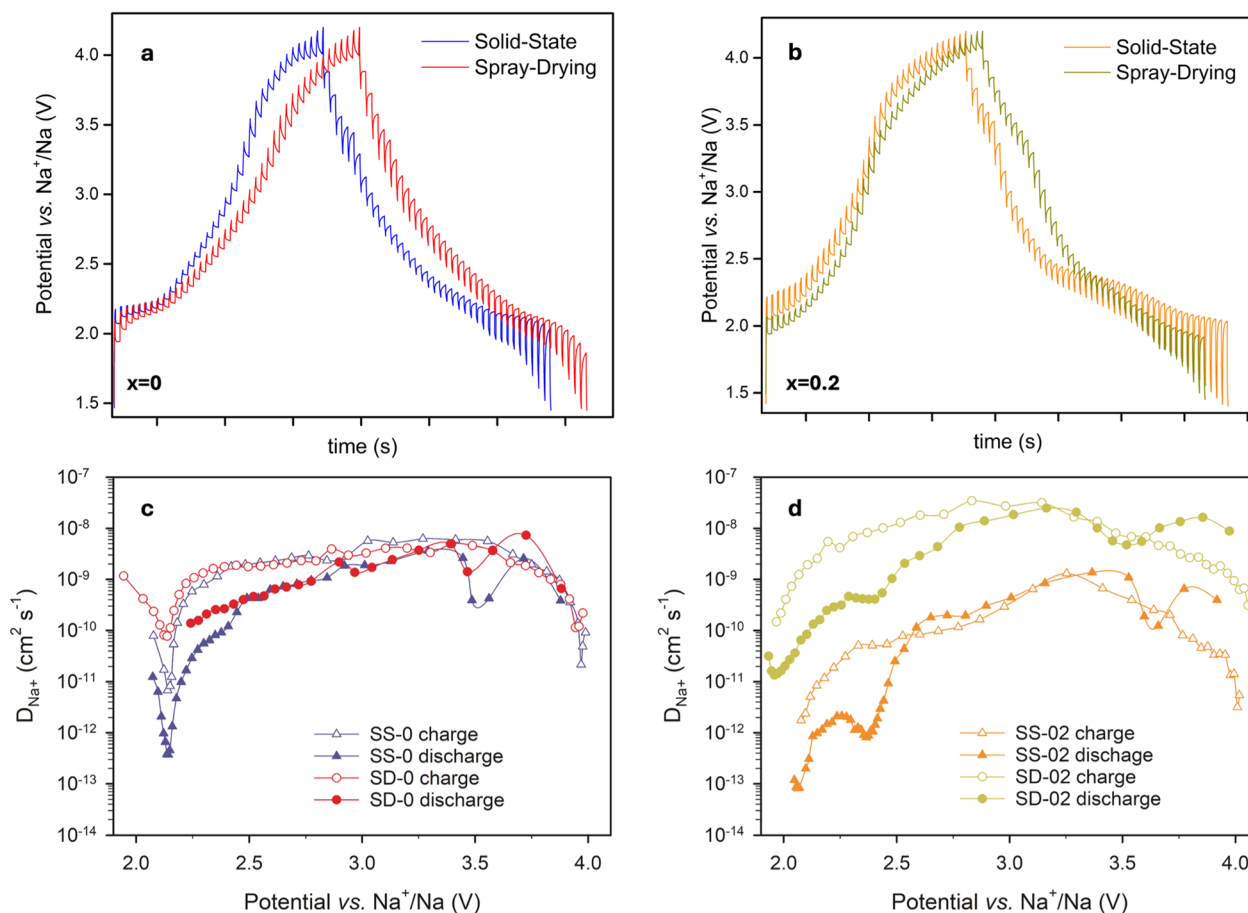

Fig. 7 GITT charge–discharge curves (@0.067C) and the calculated Na^+ diffusion coefficient (D_{Na^+}) for (a–c) $P2-Na_{0.67}Mn_{0.5}Fe_{0.5}O_2$ and (b–d) $P2-Na_{0.67}Mn_{0.5}Fe_{0.3}Mg_{0.2}O_2$.

0 and SD-0 exhibit similar D_{Na^+} during charge. However, during discharge, SD-0 demonstrates a slightly higher Na^+ diffusion, which may account for the improved performance discussed above. Nonetheless, since D_{Na^+} is consistently lower during discharge than charge, we can conclude that the Na^+ intercalation process is the rate-limiting step in the electrochemical reaction. For P2–$Na_{0.67}Mn_{0.5}Fe_{0.3}Mg_{0.2}O_2$ (Fig. 7d), the D_{Na^+} differences between the two syntheses are significantly enhanced compared to the non-substituted oxides. Interestingly, even for this composition, Na^+ insertion appears to be slower than Na^+ extraction. The most interesting result, however, is the D_{Na^+} increase by more than two orders of magnitude for SD-02 compared with SS-02. This remarkable increase can be explained by considering (i) the different microstructure of spray-dried materials compared to solid-state ones, which is inherently more suitable for the design of high-performance electrode materials; (ii) the different surface area of the two electrodes, which significantly influences the D_{Na^+} calculation; (iii) the presence of an electrochemically active impurity phase in SD-02 (O3-layered phase) compared to the inactive $FeMn_2O_4$ of SS-0, whereby only the former would contribute to the overall sodium diffusion during cycling; (iv) the coexistence of mixed P2/O3 phases for SD-02 compared to the pure P2 phase of SS-02. As previously mentioned in the Introduction, the co-existence of both P2 and O3 can, in some cases, lead to enhanced Na^+ diffusion compared to pure P2 or O3 materials, because the advantages of both phases can be fully exploited.[54] The presence of multiple interfaces in the grains composed of both P2 and O3 phases offers additional channels and active sites for enhancing the Na^+ diffusion upon cycling.[55] Due to this reason, Na^+ ions can move to and from the P2/O3-layered structure with faster kinetics and an increased diffusion rate during cycling.

3.3. *Operando* XRD

To investigate the structural evolution of the P2-layered structure during cycling and the Mg^{2+} stabilizing effect on the electrochemical properties, *operando* XRD experiments were conducted on SD-0 and SD-02. The results in Fig. 8a and b reveal that these materials exhibit different behaviors during the first two charge–discharge cycles, particularly at high potentials (>4 V). It is well-known that the biggest challenges for layered cathode materials for SIBs arise above 4 V, where the P2 structure undergoes phase transitions and structural rearrangements that, over cycling, can lead to a significant reduction in cathodic performance. These transitions occur because of the continuous Na^+ deintercalation–intercalation during cycling. This process can disrupt the structural periodicity and facilitate the formation of other inactive or unstable layered phases, such as P2′, O2, and OP4.

An observation of the 002 reflections (and also 103, 104, and 106), above 4 V, is that SD-0 undergoes the well-known P2–Z[56] phase transition, caused by the abovementioned layer sliding between the pristine P2 phase and a mixture of O2 and OP4 phases. In contrast, examination of the analogous reflections for SD-02 (Fig. 8b) reveals a consistent solid-solution-like
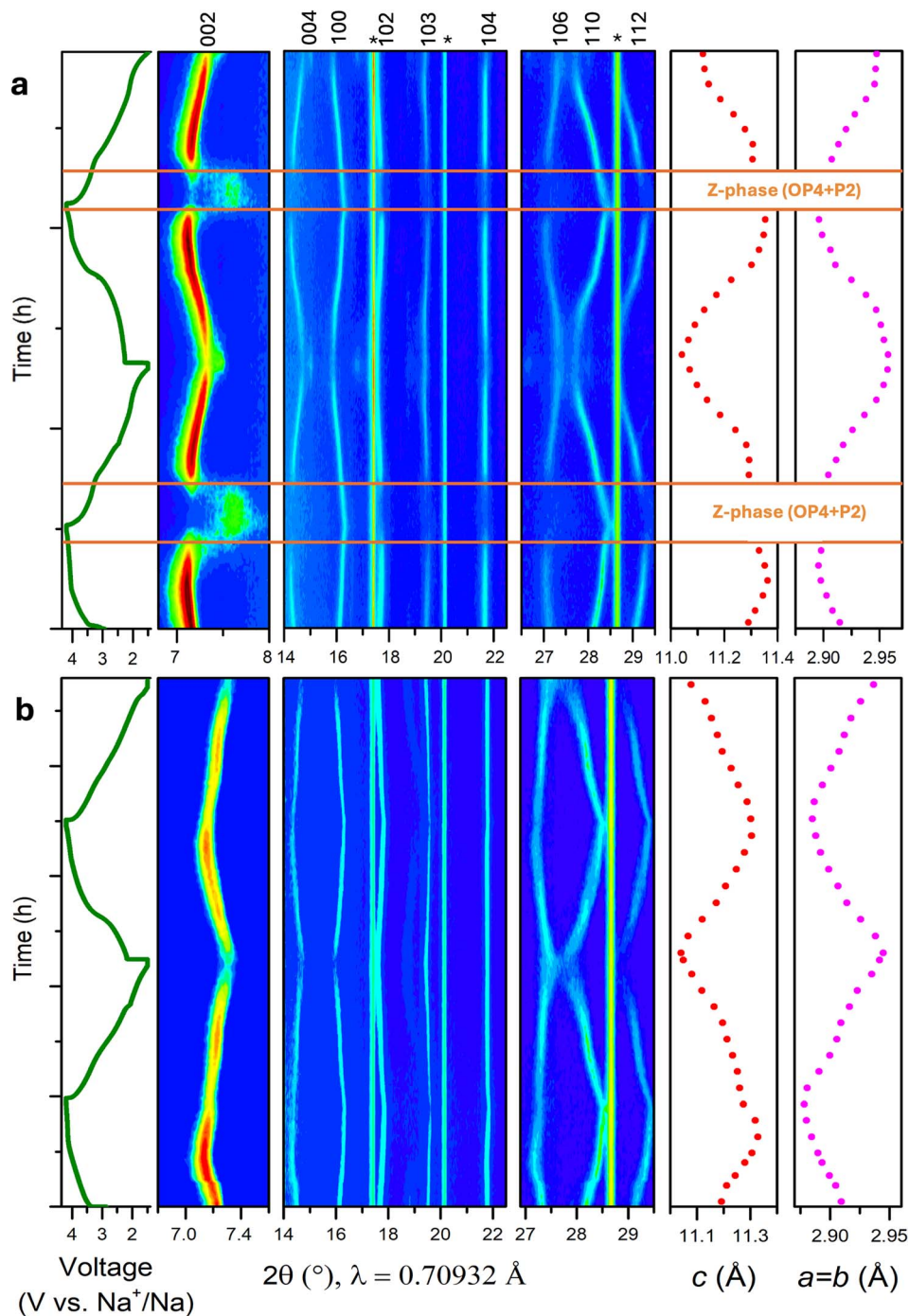
behaviour across the entire working potential range, devoid of any phase transition. Our results corroborate those by Yang *et al.*,[57] who well explained that Mg^{2+} effectively suppresses this reversible P2–OP4 phase transition.

From the 002 reflection shift, it is possible to observe the evolution of the *c* parameter, which can be easily correlated with the evolution of Na content during cycling. In particular, upon desodiation, there is initially an increase in the *c* parameter (the peak shifts to smaller angles) due to the greater repulsion between the O^{2-} present on the metal planes. This results from the reduced shielding imparted by the Na^+ ions, which migrate toward the $Na_{(m)}$ counter-electrode. Beyond a certain state of charge, the 002 reflection abruptly shifts to higher angular values, which indicates the collapse of the Na interlayer and the onset of formation of the above-mentioned Z phase. During sodiation, for the opposite reason, *c* decreases as the Na^+ ions are re-intercalated between the P2-oxide layers. 100, 110, and 112 reflections have opposite trends to those observed for 002 and can be related to *a* and *b* unit cell parameters. These two parameters decrease during charge due to the increased oxidation of metal cations, which in turn shortens the M–O bond distance,[58,59] leading to an overall contraction of the elementary cell along these directions. Fig. 8a and b also show the refined lattice parameters, obtained through LeBail refinement, during the 1st and 2nd charge–discharge cycles for SD-0 and SD-02, respectively. We decided to not refine the lattice parameters in the Z-phase potential range for SD-0 because the peaks associated with the OP4 and P2 phases are broadened by stacking faults and have low intensity, making a proper refinement cumbersome.

Notably, the *c* parameter decreases during the first charge between 4.0 V and 4.2 V for both compositions. This behavior is well-documented in layered cathode materials for LIBs (*e.g.*, LNO and NMC[60,61]) and is typically attributed to a partial collapse of layers at low Li content, leading to an overall contraction of the unit cell. In other systems, this phenomenon also overlaps with the onset of partially irreversible oxygen redox activity at high potentials, which induces local structural rearrangements and may contribute to contraction along the *c*-axis.[62] It is worth noting that, during the second cycle, this *c*-axis contraction at high potential is no longer observed, resulting in a more symmetric evolution of this cell parameter during charge and discharge. Consistent with these findings, Jin *et al.* demonstrated that for P2–$Na_{0.75}Ca_{0.04}[Li_{0.1}Ni_{0.2}Mn_{0.67}]O_2$, the asymmetry in the 00*l* reflection shift (and thus in the *c*-parameter evolution), between the end of charge and the beginning of the subsequent discharge, is attributable to O_2 formation and release.[63] This has a deleterious effect on the performance of the materials concerned.

Conversely, for both SD-0 and SD-02, the absence of this contraction at high potentials during the second cycle lends support to the hypothesis that oxygen activity and/or collapse of the layers is significantly suppressed from the second cycle onwards. In accordance with the observations above, it is evident that for both SD-0 and SD-02, the evolution trend of *c* during the second cycle exhibits a greater degree of symmetry in comparison with the initial cycle, particularly with respect to

Fig. 8 *Operando* XRD experiments performed between 1.5 V and 4.2 V for the first two charge–discharge cycles @ C/15 and the refined lattice parameter trend during the 1st and 2nd cycles for (a) SD-0 and (b) SD-02. Al (current collector) main reflections are represented by stars (*).

the relationship between charge and discharge. This is particularly clear for SD-02: c reaches its maximum value at the end of the charge (4.2 V) rather than at ~4 V, indicating that during this cycle there are practically no more irreversible contributions. Nevertheless, in order to further verify this finding, advanced RIXS and XAS measurements are required.[64,65] Furthermore, after the first and second discharge (1.5 V), a marked discrepancy in the values of c was observed between the two CAMs under investigation: values ranging from

11.041(1) Å to 11.126(2) Å for SD-0 and from 11.041(1) Å to 11.078(1) Å for SD-02 were obtained. These differences are consistent with the observations presented in Fig. S4, as the cathodes internalized less Na^+ at the end of the second discharge compared to the end of the first one. The huge divergence in these values for SD-0, compared to SD-02, further corroborates the enhanced reversibility of the Mg^{2+}-doped cathode.

4. Conclusion

In this study, we investigated the influence of different synthesis conditions and the stabilizing effect imparted by Mg(II)-doping on the electrochemical and structural properties of new cathodic materials for sodium-ion batteries. Spray-drying synthesis emerged as a promising route for preparing new cathodes, offering advantages over conventional solid-state synthesis in terms of both sustainability (lower calcination temperature and a water-based process) and functional properties. The GITT study allowed us to study the intrinsic kinetics and diffusion properties of the materials under investigation and correlate them with the observed electrochemical performance. The results of these tests, in particular concerning the η and the D_{Na^+} evolution trend analysis, allowed us to justify the significant increase in performance of the material synthesized by spray-drying compared to the solid-state synthesized material. Moreover, *operando* XRD experiments confirm the stabilizing effect of Mg^{2+} doping on the electrochemical performance of the layered oxide P2–$Na_{0.67}Mn_{0.5}Fe_{0.5}O_2$, by suppressing the reversible P2–Z phase transition occurring over 4 V, during charge, for the non-substituted oxide. Based on these findings, SD-02 demonstrated superior structural and electrochemical performance compared to the other materials. It registered more than 80 mA h g^{-1} during discharge after 200 cycles at 1C, with a capacity retention of ~70%. Moreover, we confirmed that the mixed P2/O3 phases in SD-02 are beneficial for the cathodic performances, since we take advantage of both the crystal structures' specific properties. The synergic effect between spray-drying synthesis and the doping of P2–$Na_{0.67}Mn_{0.5}Fe_{0.5}O_2$ with electrochemically inactive Mg^{2+} offers a highly effective strategy for advancing the design of new and promising cathodes. In conclusion, this integrated approach between the correct choice of the synthesis routes and the optimization of the elementary composition underscores the potential for enhancing the functional properties of the electrode materials and provides a robust framework for the development of advanced materials with improved performance. This methodology represents a promising direction for future research and commercialization of next-generation batteries.

Conflicts of interest

There are no conflicts to declare.

Data availability

All data supporting the findings of this study are included within the paper and its SI.

Supplementary information includes additional experimental spray-drying process details as well as structural–elemental and electrochemical characterization data (*e.g.*, SEM-EDX, voltage–composition profiles). See DOI: https://doi.org/10.1039/d5ta04988a.

Notes and references

1 K. Kubota, M. Dahbi, T. Hosaka, S. Kumakura and S. Komaba, Towards K-Ion and Na-Ion Batteries as "Beyond Li-Ion.", *Chem. Rec.*, 2018, **18**(4), 459–479, DOI: 10.1002/tcr.201700057.

2 K. Chayambuka, G. Mulder, D. L. Danilov and P. H. L. Notten, From Li-Ion Batteries toward Na-Ion Chemistries: Challenges and Opportunities, *Adv. Energy Mater.*, 2020, **10**(38), 2001310, DOI: 10.1002/aenm.202001310.

3 M. Walter, M. V. Kovalenko and K. V. Kravchyk, Challenges and Benefits of Post-Lithium-Ion Batteries, *New J. Chem.*, 2020, **44**(5), 1677–1683, DOI: 10.1039/c9nj05682c.

4 A. L. Lipson, B. Pan, S. H. Lapidus, C. Liao, J. T. Vaughey and B. J. Ingram, Rechargeable Ca-Ion Batteries: A New Energy Storage System, *Chem. Mater.*, 2015, **27**(24), 8442–8447, DOI: 10.1021/acs.chemmater.5b04027.

5 T. Hosaka, K. Kubota, A. S. Hameed and S. Komaba, Research Development on K-Ion Batteries, *Chem. Rev.*, 2020, **120**(14), 6358–6466, DOI: 10.1021/acs.chemrev.9b00463.

6 C. Delmas, Sodium and Sodium-Ion Batteries: 50 Years of Research, *Adv. Energy Mater.*, 2018, **8**(17), 1703137, DOI: 10.1002/aenm.201703137.

7 A. Rudola, C. J. Wright and J. Barker, Reviewing the Safe Shipping of Lithium-Ion and Sodium-Ion Cells: A Materials Chemistry Perspective, *Energy Mater. Adv.*, 2021, **2021**, 1–12, DOI: 10.34133/2021/9798460.

8 C. Fang, Y. Huang, W. Zhang, J. Han, Z. Deng, Y. Cao and H. Yang, Routes to High Energy Cathodes of Sodium-Ion Batteries, *Adv. Energy Mater.*, 2016, **6**(5), 1501727, DOI: 10.1002/aenm.201501727.

9 *CATL Unveils Its Latest Breakthrough Technology by Releasing Its First Generation of Sodium-ion Batteries*, https://www.catl.com/en/news/665.html, accessed 2024-11-15.

10 A. Rudola, A. J. R. Rennie, R. Heap, S. S. Meysami, A. Lowbridge, F. Mazzali, R. Sayers, C. J. Wright and J. Barker, Commercialisation of High Energy Density Sodium-Ion Batteries: Faradion's Journey and Outlook, *J. Mater. Chem. A*, 2021, **9**(13), 8279–8302, DOI: 10.1039/d1ta00376c.

11 I. Hasa, N. Tapia-Ruiz and M. Galceran, Editorial: Sodium-Ion Batteries: From Materials Discovery and Understanding to Cell Development, *Front. Energy Res.*, 2022, **10**, 1076764, DOI: 10.3389/fenrg.2022.1076764.

12 P. Gupta, S. Pushpakanth, M. A. Haider and S. Basu, Understanding the Design of Cathode Materials for Na-Ion Batteries, *ACS Omega*, 2022, 7(7), 5605–5614, DOI: 10.1021/acsomega.1c05794.

13 P. F. Wang, Y. You, Y. X. Yin and Y. G. Guo, Layered Oxide Cathodes for Sodium-Ion Batteries: Phase Transition, Air Stability, and Performance, *Adv. Energy Mater.*, 2018, **8**(8), 1701912, DOI: 10.1002/aenm.201701912.

14 W. Zuo, J. Qiu, X. Liu, F. Ren, H. Liu, H. He, C. Luo, J. Li, G. F. Ortiz, H. Duan, J. Liu, M. S. Wang, Y. Li, R. Fu and

Y. Yang, The Stability of P2-Layered Sodium Transition Metal Oxides in Ambient Atmospheres, *Nat. Commun.*, 2020, **11**, 3544, DOI: **10.1038/s41467-020-17290-6**.

15 J. Peng, W. Zhang, Q. Liu, J. Wang, S. Chou, H. Liu and S. Dou, Prussian Blue Analogues for Sodium-Ion Batteries: Past, Present, and Future, *Adv. Mater.*, 2022, **34**(15), 2108384, DOI: **10.1002/adma.202108384**.

16 Y. Lyu, X. Wu, K. Wang, Z. Feng, T. Cheng, Y. Liu, M. Wang, R. Chen, L. Xu, J. Zhou, Y. Lu and B. Guo, An Overview on the Advances of $LiCoO_2$ Cathodes for Lithium-Ion Batteries, *Adv. Energy Mater.*, 2021, **11**(2), 1–29, DOI: **10.1002/aenm.202000982**.

17 K. Mizushima, P. C. Jones, P. J. Wiseman and J. B. Goodenough, Li_xCoO_2 (0<x<-1): A New Cathode Material for Batteries of High Energy Density, *Mater. Res. Bull.*, 1980, **15**, 783–789.

18 C. Delmas, C. Fouassier and P. Hagenmuller, Structural Classification and Properties of the Layered Oxides, *Physica B+C*, 1980, **99**, 81–85.

19 W. K. Pang, S. Kalluri, V. K. Peterson, N. Sharma, J. Kimpton, B. Johannessen, H. K. Liu, S. X. Dou and Z. Guo, Interplay between Electrochemistry and Phase Evolution of the P2-Type $Na_x(Fe_{1/2}Mn_{1/2})O_2$ Cathode for Use in Sodium-Ion Batteries, *Chem. Mater.*, 2015, **27**(8), 3150–3158, DOI: **10.1021/acs.chemmater.5b00943**.

20 Q. Yang, P. F. Wang, J. Z. Guo, Z. M. Chen, W. L. Pang, K. C. Huang, Y. G. Guo, X. L. Wu and J. P. Zhang, Advanced $P2-Na_{2/3}Ni_{1/3}Mn_{7/12}Fe_{1/12}O_2$ Cathode Material with Suppressed P2-O2 Phase Transition toward High-Performance Sodium-Ion Battery, *ACS Appl. Mater. Interfaces*, 2018, **10**(40), 34272–34282, DOI: **10.1021/acsami.8b12204**.

21 W. Zuo, Z. Xiao, M. Zarrabeitia, X. Xue, Y. Yang and S. Passerini, Guidelines for Air-Stable Lithium/Sodium Layered Oxide Cathodes, *ACS Mater. Lett.*, 2022, **4**(6), 1074–1086, DOI: **10.1021/acsmaterialslett.1c00827**.

22 Y. Huang, W. Zhang, Y. Zhou, Y. Wang, L. Li, H. Shao, X. Li, Z. Hong, H. Xia, Y. Shen and L. Chen, Air Corrosion of Layered Cathode Materials for Sodium-Ion Batteries: Cation Mixing and a Practical Suppression Strategy, *ACS Nano*, 2024, **18**(20), 13106–13116, DOI: **10.1021/acsnano.4c01962**.

23 D. Darbar, N. Muralidharan, R. P. Hermann, J. Nanda and I. Bhattacharya, Evaluation of Electrochemical Performance and Redox Activity of Fe in Ti Doped Layered $P2-Na_{0.67}Mn_{0.5}Fe_{0.5}O_2$ Cathode for Sodium Ion Batteries, *Electrochim. Acta*, 2021, **380**, 138156, DOI: **10.1016/j.electacta.2021.138156**.

24 Z. Cheng, B. Zhao, Y. J. Guo, L. Yu, B. Yuan, W. Hua, Y. X. Yin, S. Xu, B. Xiao, X. Han, P. F. Wang and Y. G. Guo, Mitigating the Large-Volume Phase Transition of P2-Type Cathodes by Synergetic Effect of Multiple Ions for Improved Sodium-Ion Batteries, *Adv. Energy Mater.*, 2022, **12**(14), 2103461, DOI: **10.1002/aenm.202103461**.

25 S. C. Han, H. Lim, J. Jeong, D. Ahn, W. B. Park, K. S. Sohn and M. Pyo, Ca-Doped Na_xCoO_2 for Improved Cyclability in Sodium Ion Batteries, *J. Power Sources*, 2015, **277**, 9–16, DOI: **10.1016/j.jpowsour.2014.11.150**.

26 Q. C. Wang, J. K. Meng, X. Y. Yue, Q. Q. Qiu, Y. Song, X. J. Wu, Z. W. Fu, Y. Y. Xia, Z. Shadike, J. Wu, X. Q. Yang and Y. N. Zhou, Tuning P2-Structured Cathode Material by Na-Site Mg Substitution for Na-Ion Batteries, *J. Am. Chem. Soc.*, 2019, **141**(2), 840–848, DOI: **10.1021/jacs.8b08638**.

27 P. Wang, Y. You, Y. Yin, Y. Wang, L. Wan, L. Gu and Y. Guo, Suppressing the P2–O2 Phase Transition of $Na_{0.67}Mn_{0.67}Ni_{0.33}O_2$ by Magnesium Substitution for Improved Sodium-Ion Batteries, *Angew. Chem.*, 2016, **128**(26), 7571–7575, DOI: **10.1002/ange.201602202**.

28 N. Yabuuchi, R. Hara, K. Kubota, J. Paulsen, S. Kumakura and S. Komaba, A New Electrode Material for Rechargeable Sodium Batteries: P2-Type $Na_{2/3}[Mg_{0.28}Mn_{0.72}]O_2$ with Anomalously High Reversible Capacity, *J. Mater. Chem. A*, 2014, **2**(40), 16851–16855, DOI: **10.1039/c4ta04351k**.

29 B. S. Kumar, R. Kumar, A. Pradeep, A. Amardeep, V. Srihari, H. K. Poswal, A. Chatterjee and A. Mukhopadhyay, Fundamental Principles toward Designing High Na-Containing P2-Structured "Layered" Na-Transition Metal Oxides as High-Performance Cathode Materials for Na-Ion Batteries, *Chem. Mater.*, 2022, **34**(23), 10470–10483, DOI: **10.1021/acs.chemmater.2c02478**.

30 V. K. Kumar, S. Ghosh, S. Biswas and S. K. Martha, P2-Type $Na_{0.67}Mn_{0.5}Fe_{0.5}O_2$ Synthesized by Solution Combustion Method as an Efficient Cathode Material for Sodium-Ion Batteries, *J. Electrochem. Soc.*, 2021, **168**(3), 030512, DOI: **10.1149/1945-7111/abe985**.

31 K. Park, D. Han, H. Kim, W. S. Chang, B. Choi, B. Anass and S. Lee, Characterization of a P2-Type Chelating-Agent-Assisted $Na_{2/3}Fe_{1/2}Mn_{1/2}O_2$ Cathode Material for Sodium-Ion Batteries, *RSC Adv.*, 2014, **4**(43), 22798–22802, DOI: **10.1039/c4ra01391c**.

32 S. Altin, E. Altundag, E. Altin and S. Altundag, Improved Battery Performance of Silicon Modified $Na_{0.67}Fe_{0.5}Mn_{0.5}O_2$ and Its Structural and Electrochemical Properties: An Investigation of Infrared Thermal Imaging, *J. Energy Storage*, 2021, **41**, 102979, DOI: **10.1016/j.est.2021.102979**.

33 S. Altin, S. Altundag, E. Altin, E. Oz, M. Harfouche and A. Bayri, Investigation of Ti-Substitution Effects on Structural and Electrochemical Properties of $Na_{0.67}Mn_{0.5}Fe_{0.5}O_2$ Battery Cells, *Int. J. Energy Res.*, 2020, **44**(14), 11794–11806, DOI: **10.1002/er.5820**.

34 B. Vertruyen, N. Eshraghi, C. Piffet, J. Bodart, A. Mahmoud and F. Boschini, Spray-Drying of Electrode Materials for Lithium- and Sodium-Ion Batteries, *Materials*, 2018, **11**(7), 1076, DOI: **10.3390/ma11071076**.

35 D. S. Jung, S. B. Park and Y. C. Kang, Design of Particles by Spray Pyrolysis and Recent Progress in Its Application, *Korean J. Chem. Eng.*, 2010, **27**(6), 1621–1645, DOI: **10.1007/s11814-010-0402-5**.

36 G. L. Messing, S.-C. Zhang and G. V. Jayanthi, Ceramic Powder Synthesis by Spray Pyrolysis, *J. Am. Ceram. Soc.*, 1993, **76**(11), 2707.

37 M. Xu, G. Gammaitoni, M. Häfner, E. Villalobos-Portillo, C. Marini and M. Bianchini, Understanding and

Optimizing Li Substitution in P2-Type Sodium Layered Oxides for Sodium-Ion Batteries, *Adv. Funct. Mater.*, 2025, 2425499, DOI: **10.1002/adfm.202425499**.

38 N. Yabuuchi, M. Kajiyama, J. Iwatate, H. Nishikawa, S. Hitomi, R. Okuyama, R. Usui, Y. Yamada and S. Komaba, P2-Type $Na_x[Fe_{1/2}Mn_{1/2}]O_2$ Made from Earth-Abundant Elements for Rechargeable NaÂ Batteries, *Nat. Mater.*, 2012, **11**(6), 512–517, DOI: **10.1038/nmat3309**.

39 S. Komaba, T. Ishikawa, N. Yabuuchi, W. Murata, A. Ito and Y. Ohsawa, Fluorinated Ethylene Carbonate as Electrolyte Additive for Rechargeable Na Batteries, *ACS Appl. Mater. Interfaces*, 2011, **3**(11), 4165–4168, DOI: **10.1021/am200973k**.

40 Y. Lee, J. Lee, H. Kim, K. Kang and N. S. Choi, Highly Stable Linear Carbonate-Containing Electrolytes with Fluoroethylene Carbonate for High-Performance Cathodes in Sodium-Ion Batteries, *J. Power Sources*, 2016, **320**, 49–58, DOI: **10.1016/j.jpowsour.2016.04.070**.

41 Z. Chen, M. Yang, G. Chen, G. Tang, Z. Huang, M. Chu, R. Qi, S. Li, R. Wang, C. Wang, T. Zhang, J. Zhai, W. Zhao, J. Zhang, J. Chen, L. He, J. Xu, W. Yin, J. Wang and Y. Xiao, Triggering Anionic Redox Activity in Fe/Mn-Based Layered Oxide for High-Performance Sodium-Ion Batteries, *Nano Energy*, 2022, **94**, 106958, DOI: **10.1016/j.nanoen.2022.106958**.

42 J. Jin, Y. Liu, Q. Shen, X. Zhao, J. Zhang, Y. Song, T. Li, X. Xing and J. Chen, Unveiling the Complementary Manganese and Oxygen Redox Chemistry for Stabilizing the Sodium-Ion Storage Behaviors of Layered Oxide Cathodes, *Adv. Funct. Mater.*, 2022, **32**(29), 2203424, DOI: **10.1002/adfm.202203424**.

43 C. Cheng, M. Ding, T. Yan, K. Dai, J. Mao, N. Zhang, L. Zhang and J. Guo, Exploring the Charge Compensation Mechanism of P2-Type $Na_{0.6}Mg_{0.3}Mn_{0.7}O_2$ Cathode Materials for Advanced Sodium-Ion Batteries, *Energies*, 2020, **13**(21), 5729, DOI: **10.3390/en13215729**.

44 A. Rudola, D. Aurbach and P. Balaya, A New Phenomenon in Sodium Batteries: Voltage Step Due to Solvent Interaction, *Electrochem. Commun.*, 2014, **46**, 56–59, DOI: **10.1016/j.elecom.2014.06.008**.

45 M. Akhtar, H. Arraghraghi, S. Kunz, Q. Wang and M. Bianchini, A Novel Solid-State Synthesis Route for High Voltage $Na_3V_2(PO_4)_2F_{3-2y}O_{2y}$ Cathode Materials for Na-Ion Batteries, *J. Mater. Chem. A*, 2023, **11**(46), 25650–25661, DOI: **10.1039/d3ta04239a**.

46 D. Zhou, W. Huang, X. Lv and F. A. Zhao, Novel P2/O3 Biphase $Na_{0.67}Fe_{0.425}Mn_{0.425}Mg_{0.15}O_2$ as Cathode for High-Performance Sodium-Ion Batteries, *J. Power Sources*, 2019, **421**, 147–155, DOI: **10.1016/j.jpowsour.2019.02.061**.

47 L. Yu, Z. Cheng, K. Xu, Y. X. Chang, Y. H. Feng, D. Si, M. Liu, P. F. Wang and S. Xu, Interlocking Biphasic Chemistry for High-Voltage P2/O3 Sodium Layered Oxide Cathode, *Energy Storage Mater.*, 2022, **50**, 730–739, DOI: **10.1016/j.ensm.2022.06.012**.

48 Y. Jiang, W. Li and K. Luo, Solid-Solution Reaction and Ultrasmall Volume Change in High-Entropy P2-Type Layered Oxide Cathode for All-Climate Sodium-Ion Batteries, *ACS Sustain. Chem. Eng.*, 2024, **12**(21), 8051–8060, DOI: **10.1021/acssuschemeng.4c00185**.

49 G. Zhang, J. Li, Y. Fan, Y. Liu, P. Zhang, X. Shi, J. Ma, R. Zhang and Y. Huang, Suppressed P2–P2′ Phase Transition of Fe/Mn-Based Layered Oxide Cathode for High-Performance Sodium-Ion Batteries, *Energy Storage Mater.*, 2022, **51**, 559–567, DOI: **10.1016/j.ensm.2022.06.045**.

50 W. Weppner and R. A. Huggins, Determination of the Kinetic Parameters of Mixed Conducting Electrodes and Application to the System LLSb, *J. Electrochem. Soc.: Solid-State Sci. Technol.*, 1977, **124**(10), 1569–1578.

51 B. Zhou, D. Wong, Z. Fu, H. Guo, C. Schulz, G. Karkera, H. Hahn, M. Bianchini and Q. Wang, K-Doping Suppresses Oxygen Redox in P2-$Na_{0.67}Ni_{0.11}Cu_{0.22}Mn_{0.67}O_2$ Cathode Materials for Sodium-Ion Batteries, *Small*, 2024, **20**(43), 2402991, DOI: **10.1002/smll.202402991**.

52 Q. C. Wang, Z. Shadike, X. L. Li, J. Bao, Q. Q. Qiu, E. Hu, S. M. Bak, X. Xiao, L. Ma, X. J. Wu, X. Q. Yang and Y. N. Zhou, Tuning Sodium Occupancy Sites in P2-Layered Cathode Material for Enhancing Electrochemical Performance, *Adv. Energy Mater.*, 2021, **11**(13), 2003455, DOI: **10.1002/aenm.202003455**.

53 E. Deiss, Spurious Chemical Diffusion Coefficients of Li^+ in Electrode Materials Evaluated with GITT, *Electrochim. Acta*, 2005, **50**(14), 2927–2932, DOI: **10.1016/j.electacta.2004.11.042**.

54 E. Grépin, I. A. Moiseev, A. M. Abakumov, J.-M. Tarascon and S. Mariyappan, Rational Selection of Sodium Layered Oxides for High Performance Na-Ion Batteries: P2 vs O3 vs P2-O3 Intergrowths, *J. Electrochem. Soc.*, 2023, **170**(8), 080510, DOI: **10.1149/1945-7111/acec66**.

55 G. Gao, D. Tie, H. Ma, H. Yu, S. Shi, B. Wang, S. Xu, L. Wang and Y. Zhao, Interface-Rich Mixed P2 + T Phase $Na_xCo_{0.1}Mn_{0.9}O_2$ ($0.44 \leq x \leq 0.7$) toward Fast and High Capacity Sodium Storage, *J. Mater. Chem. A*, 2018, **6**(15), 6675–6684, DOI: **10.1039/c8ta00206a**.

56 J. W. Somerville, A. Sobkowiak, N. Tapia-Ruiz, J. Billaud, J. G. Lozano, R. A. House, L. C. Gallington, T. Ericsson, L. Häggström, M. R. Roberts, U. Maitra and P. G. Bruce, Nature of the "z"-Phase in Layered Na-Ion Battery Cathodes, *Energy Environ. Sci.*, 2019, **12**(7), 2223–2232, DOI: **10.1039/c8ee02991a**.

57 J. Yang, A. E. Maughan, G. Teeter, B. J. Tremolet de Villers, S. M. Bak and S. D. Han, Structural Stabilization of P2-Type Sodium Iron Manganese Oxides by Electrochemically Inactive Mg Substitution: Insights of Redox Behavior and Voltage Decay, *ChemSusChem*, 2020, **13**(22), 5972–5982, DOI: **10.1002/cssc.202001963**.

58 Z. Lu and J. R. Dahn, In Situ X-Ray Diffraction Study of P2-$Na_{2/3}[Ni_{1/3}Mn_{2/3}]O_2$, *J. Electrochem. Soc.*, 2001, **148**(11), A1225–A1229, DOI: **10.1149/1.1407247**.

59 H. Liu, X. Gao, J. Chen, J. Gao, S. Yin, S. Zhang, L. Yang, S. Fang, Y. Mei, X. Xiao, L. Chen, W. Deng, F. Li, G. Zou, H. Hou and X. Ji, Reversible OP4 Phase in P2–$Na_{2/3}Ni_{1/3}Mn_{2/3}O_2$ Sodium Ion Cathode, *J. Power Sources*, 2021, **508**, 230324, DOI: **10.1016/j.jpowsour.2021.230324**.

60 M. Mock, M. Bianchini, F. Fauth, K. Albe and S. Sicolo, Atomistic Understanding of the $LiNiO_2$-NiO_2 phase Diagram from Experimentally Guided Lattice Models, *J.*

Mater. Chem. A, 2021, **9**(26), 14928–14940, DOI: **10.1039/d1ta00563d**.

61 L. De Biasi, A. O. Kondrakov, H. Geßwein, T. Brezesinski, P. Hartmann and J. Janek, Between Scylla and Charybdis: Balancing among Structural Stability and Energy Density of Layered NCM Cathode Materials for Advanced Lithium-Ion Batteries, *J. Phys. Chem. C*, 2017, **121**(47), 26163–26171, DOI: **10.1021/acs.jpcc.7b06363**.

62 A. Konarov, H. J. Kim, J. H. Jo, N. Voronina, Y. Lee, Z. Bakenov, J. Kim and S. T. Myung, High-Voltage Oxygen-Redox-Based Cathode for Rechargeable Sodium-Ion Batteries, *Adv. Energy Mater.*, 2020, **10**(24), 2001111, DOI: **10.1002/aenm.202001111**.

63 J. Jin, Y. Liu, Q. Shen, X. Zhao, J. Zhang, Y. Song, T. Li, X. Xing and J. Chen, Unveiling the Complementary Manganese and Oxygen Redox Chemistry for Stabilizing the Sodium-Ion Storage Behaviors of Layered Oxide Cathodes, *Adv. Funct. Mater.*, 2022, **32**(29), 2203424, DOI: **10.1002/adfm.202203424**.

64 E. Boivin, R. A. House, M. A. Pérez-Osorio, J. J. Marie, U. Maitra, G. J. Rees and P. G. Bruce, Bulk O_2 Formation and Mg Displacement Explain O-Redox in $Na_{0.67}Mn_{0.72}Mg_{0.28}O_2$, *Joule*, 2021, **5**(5), 1267–1280, DOI: **10.1016/j.joule.2021.04.006**.

65 I. Abate, S. Y. Kim, C. D. Pemmaraju, M. F. Toney, W. Yang, T. P. Devereaux, W. C. Chueh and L. F. Nazar, The Role of Metal Substitution in Tuning Anion Redox in Sodium Metal Layered Oxides Revealed by X-Ray Spectroscopy and Theory, *Angew. Chem., Int. Ed.*, 2021, **60**(19), 10880–10887, DOI: **10.1002/anie.202012205**.